Letter

Anomalous bond softening mediated by strain-induced Friedel-like oscillations in a BC$_2$N superlattice

Tengfei Xu,[1,2] Zhaorui Liu,[1,2] Dominik Legut [3,4] and Ruifeng Zhang [1,2,*]

[1]*School of Materials Science and Engineering, Beihang University, Beijing 100191, People's Republic of China*
[2]*Center for Integrated Computational Engineering (International Research Institute for Multidisciplinary Science) and Key Laboratory of High-Temperature Structural Materials & Coatings Technology (Ministry of Industry and Information Technology), Beihang University, Beijing 100191, People's Republic of China*
[3]*IT4Innovations, VSB-Technical University of Ostrava, 17. listopadu 2172/15, 708 00 Ostrava, Czech Republic*
[4]*Nanotechnology Center, CEET, VSB-Technical University of Ostrava, 17. listopadu 2172/15, 708 00 Ostrava, Czech Republic*

The crystal structure of BC$_2$N and the origin of its superhardness remain under constant debate, hindering its development. Herein, by evaluating the x-ray diffraction pattern, the thermodynamic stability at normal and high pressures of a series of BC$_2$N candidates, the (111) BC$_2$N$_{2\times2}$ superlattice (labeled R2u−BC$_2$N) is identified as the realistic crystal structure of the experimentally synthesized BC$_2$N. We further reveal that the strain-induced Friedel-like oscillations dominates the preferable slip systems of R2u−BC$_2$N by drastically weakening the heterogenous bonds across the slip plane and thus leads to its ultralow dislocation slip resistance, which originates from the metallization triggered by the reduction in energy separation between bonding and antibonding interactions of the softened bonds. Our results rule out R2u−BC$_2$N as the intrinsic superhard material surpassing c-BN, whereas the experimentally determined extreme hardness can be attributed to the nanocrystalline grains glued by interfacial amorphous carbon which provides a strong barrier for plastic deformation. These findings provide a view of the longstanding issue of the possible structure of experimentally observed BC$_2$N, and establish a mechanism underlying the strain-driven electronic instability of superlattice structures, providing guidance towards rational design of superhard materials.

Superhard B-C-N ternary compounds have gained significant interest because of their unique thermodynamic and mechanical properties as well as numerous potential applications [1–6]. However, unresolved challenges regarding their theoretical and experimental aspects hinder their development. The successful synthesis of single BC$_2$N phase at high pressure [7,8] initiated a longstanding disagreement regarding its actual crystal structure, i.e., whether carbon can be randomly distributed in BN lattice or vice versa because they are thermodynamically immiscible with minor lattice mismatch [9,10]. Although experimentally synthesized BC$_2$N was reported to possess extreme hardness, the origin of its superhardness remains under debate [9–13]. This is because the plasticity might shift from crystal's inside to interface when the crystalline size approaches the nanometer scale, eventually inducing the strongest size effect [6,14,15], yet these facts are generally ignored in previous studies.

Generally, two classes of candidate structures have been proposed to fit the experimentally synthesized BC$_2$N by reproducing experimentally determined x-ray diffraction (XRD) patterns and following calculated formation enthalpy under ambient conditions. The first class includes substitutional solid solutions with diamondlike parent lattices, e.g., BC$_2$N−n (n = 1–7) [16], t-BC$_2$N, z-BC$_2$N, and z*-BC$_2$N

[17,18]. Although these structures provide somehow consistence to the XRD patterns, minor deviation still exists, challenging the rationality of these structures, yet this agree with the high formation enthalpy of these compounds under ambient conditions. To account for this deficiency, Chen *et al.* [12], Li *et al.* [19] and Liu *et al.* [20] successively suggested the second-class candidates, i.e., (111) superlattice structures formed by sequentially stacking c-BN and diamond layers, which have better thermodynamic stability than the solution types because of the immiscible feature between c-BN and diamond under ambient conditions. However, the formation enthalpy under ambient conditions does not guarantee the stability at high pressure (i.e., the real experimental pressure ~20 GPa for BC$_2$N) which might stabilize some novel unstable/metastable structures via lattice distortion involving the local bond twisting, rotating, and even reconstruction.

Regarding the origin of the extreme hardness of BC$_2$N, it is believed that the disordering of BC$_2$N solid solution may induce strength enhancement owing to the random distribution of C-C bonds that are stronger than B-N bonds, and consequently this was used to explain the intrinsic superhardness of BC$_2$N [17,18]. Unfortunately, this explanation is only plausible if the structure of BC$_2$N is determined to be a solid solution, whereas the fact that the formation enthalpy of BC$_2$N solid solution is higher than that of BC$_2$N superlattice under ambient conditions does not seem to support this type of structure. In BC$_2$N superlattice, the periodic heterogenous interfaces formed by the ordered alignment of

---

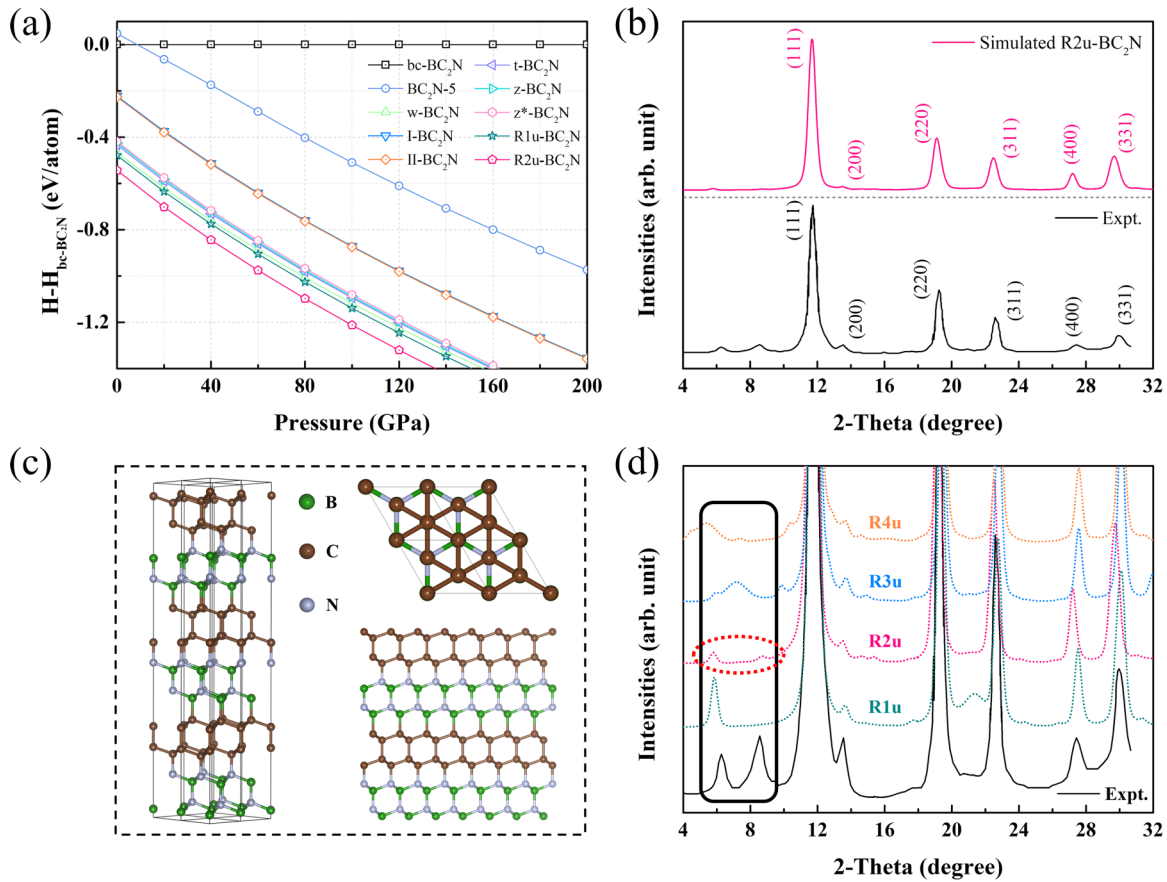*Corresponding author: zrf@buaa.edu.cn

FIG. 1. (a) Relative enthalpy vs pressure for BC_2N. bc-BC_2N is taken as reference. (b) Simulated XRD patterns of $R2u-BC_2N$ and experimental pattern reproduced from Ref. [8]. (c) Crystal structure of $R2u-BC_2N$. (d) Enlarged diffraction peaks of simulated XRD patterns of $Rnu-BC_2N$ ($n = 1$–4) and experimental pattern reproduced from Ref. [8].

B-N and C-C bonds may cause peculiar electronic behavior, e.g., charge perturbations observed in nanotwinned c-BN [21] and TmN/SiNx nanocomposite systems [22], which would also significantly affect the mechanical strength. Considering BC_2N superlattice is the most realistic experimentally synthesized BC_2N, we need to clarify whether BC_2N is an intrinsic superhard material exceeding c-BN or not, and the origin of its experimentally observed superior hardness. This requires a more realistic justification based on both the intrinsic plastic resistance of constitute crystal and the nano-size effects tuned by strongly bonded interface, because these two aspects may compete to serve as the major plastic and fracture mechanisms for the experimentally synthesized nanostructured BC_2N.

Here we show that superlattice structures maintain the optimal thermodynamic stability from normal to high pressures compared to any solid solutions, and the $R2u-BC_2N$ is further verified as the synthesized BC_2N phase not only based on its stability, but also by its perfectly reproduced XRD pattern. By comparing the plastic descriptors, such as ideal strength [23,24] and Peierls stress [25,26], of $R2u-BC_2N$ and c-BN under various deformation conditions, it is surprisingly found that the Friedel-like oscillations of valence charge density remarkably limit the dislocation slip resistance of $R2u-BC_2N$ by softening the heterogenous bonds across the slip plane. Through large scale atomistic simulations, we demonstrate further that the interfacial amorphous carbon, rather than the

crystal's inside, dominates the plastic flow in nanostructured BC_2N, providing a realistic explanation for the measured extreme hardness, albeit weak bonding nature of $R2u-BC_2N$.

Thermodynamic stability at normal pressure does not guarantee the stability at high pressure because pressure will fundamentally change the stability sequence of different phases depending on their formation enthalpy. However, since its discovery through high pressure experiments, the possible structures of BC_2N were proposed based on the energetic stability under ambient conditions, while neglecting the pressure contributions. To demonstrate the real candidate of BC_2N, we systematically investigated the pressure-dependent thermodynamic stabilities of two short period (111) BC_2N superlattices (i.e., R1u-BC_2N and $R2u-BC_2N$), and those of several substitutional solutions proposed in previous studies [12,16,18,27–29] [Fig. 1(a)]. It is clearly seen that two BC_2N superlattices possess the lowest formation enthalpy among all the proposed candidates under zero pressure, which is consistent with theoretical calculations [12,19,20]. As the pressure increases from 0 to 200 GPa, the superlattice $R2u-BC_2N$ remains the most energetically stable phase, with formation enthalpies much lower than those of the solutions and $\sim$0.07 eV/atom lower than that of R1u-BC_2N at an experimental pressure of 20 GPa [8]. The XRD pattern of $R2u-BC_2N$ was simulated with x-ray wavelength $\lambda = 0.424$ Å and grain size $d = 5$ nm, which are identical to
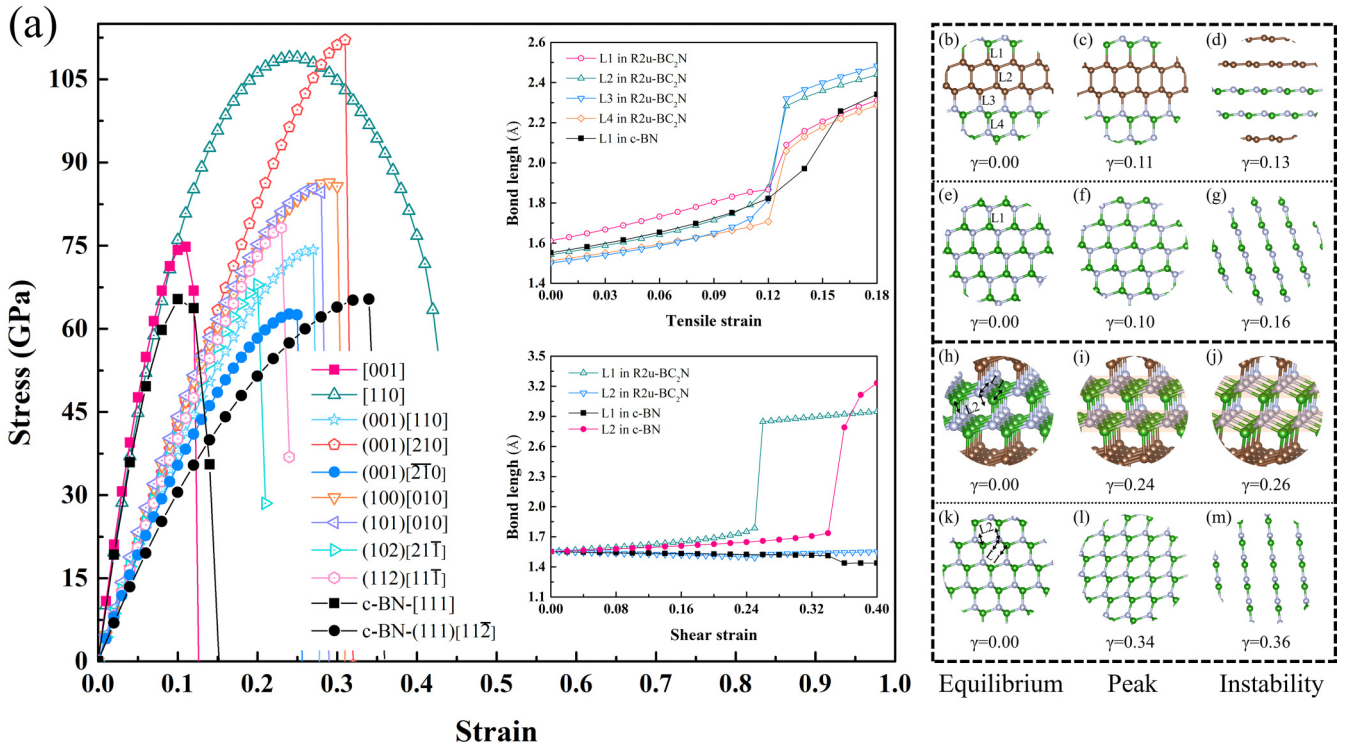
FIG. 2. (a) Tensile and shear stress-strain curves of R2u−BC$_2$N, and those of c-BN along its weakest tensile direction and shear path. Insets shows the key bond lengths (marked as "L1" to "L4") variations in R2u−BC$_2$N and c-BN under tensile and shear strains. Snapshots of deformed structures at equilibrium, peak and instability strains: (b)–(d) R2u−BC$_2$N and (e)–(g) c-BN under tensile strains, (h)–(j) R2u−BC$_2$N and (k)–(m) c-BN under shear strains. The structure transformation of B-N layers in R2u−BC$_2$N under shear loading are highlighted as pale brown areas.

the experimental conditions [8]. Obviously, all the simulated diffraction peaks for R2u−BC$_2$N show excellent agreement with the experimental ones [Fig. 1(b)] that can be seen as the stacking of two layers of c-BN and two double layers of diamond as illustrated in Fig. 1(c). It is interestingly found further that the total energy decreases as the number of stacking layers (i.e., superlattice period) increases, suggesting that the longer period structures are more energetically favored than R2u−BC$_2$N [9,12]. Nevertheless, the simulated XRD patterns of the other superlattice candidates do not match the experimental XRD pattern, which shows two significant deviations between 5° and 10° [Fig. 1(d)], disqualifying them as BC$_2$N candidates. The lattice stability of R2u−BC$_2$N is further evaluated. In Fig. S2, the phonon dispersions at pressures from 0 to 20 GPa are positive for all wave vectors in the whole Brillouin zone, i.e., no imaginary modes are present, indicating its dynamical stability at zero and high pressures. Additionally, the mechanical stability of R2u−BC$_2$N is corroborated by calculating its single-crystal elastic constants at zero and high pressures, all of which satisfy the elastic stability criterion [30,31] (Table S1 in the Supplemental Material [32], Refs. [14,24,25,31,33–63]). Hence, the superlattice R2u−BC$_2$N represents the most realistic crystal structure of the experimentally synthesized BC$_2$N, which supports the findings of Li *et al.* [19] albeit the pressure dependence being neglected for the latter.

The intrinsic lattice and extrinsic microscopic contributions [14] were considered simultaneously to obtain a realistic quantification of the mechanistic origin of the BC$_2$N

superhardness. We first demonstrate the former by comparing the calculated ideal strength, ideal cleavage/slide stress, and Peierls stress. Figure 2(a) shows the anisotropic stress-strain relationships of R2u−BC$_2$N under various affine tension and shear loadings. The tensile stress of R2u−BC$_2$N along the [001] direction exhibits the lowest peak value (74.8 GPa), which is higher than that of c-BN (65.4 GPa) along the [111] direction. The bond length variations under the [001] strain clearly show that, while the four non-equivalent bonds ["L1" to "L4" in Fig. 2(b)] weaken with increasing strain and break at the same strain of 0.13, "L3" (1.51 Å) and "L4" (1.50 Å) are much shorter than the B-N bond (1.55 Å) in c-BN ["L1" in Fig. 2(e)] under equilibrium condition. This characteristic is maintained for a wide strain range of 0.00–0.12, indicating these two stronger bonds are the main load-bearing units resisting the applied strain, thereby producing a larger tensile stress than that of c-BN. A similar stacking sequence between (001) of R2u−BC$_2$N and (111) of c-BN allows similar breakage modes under tensile deformation [Figs. 2(d) and 2(g)], i.e., strain-induced graphitization [64,65]. Interestingly, along the weakest (001) [$\bar{2}$10] shear path, the ideal shear strength of R2u−BC$_2$N (62.7 GPa) is slightly lower than that of c-BN (65.3 GPa). This originates from the more profound softening of B-N bond in its B-N layers than B-N bond in c-BN when strain increases, i.e., the bond length of "L1" in R2u−BC$_2$N [Fig. 2(h)] increased by 0.23 Å when the strain increases from 0.00 to 0.24, whereas that of "L2" in c-BN increased by 0.10 Å [Fig. 2(k)]. In stark contrast to the lattice instability mode of c-BN, "L1" in R2u−BC$_2$N immediately breaks
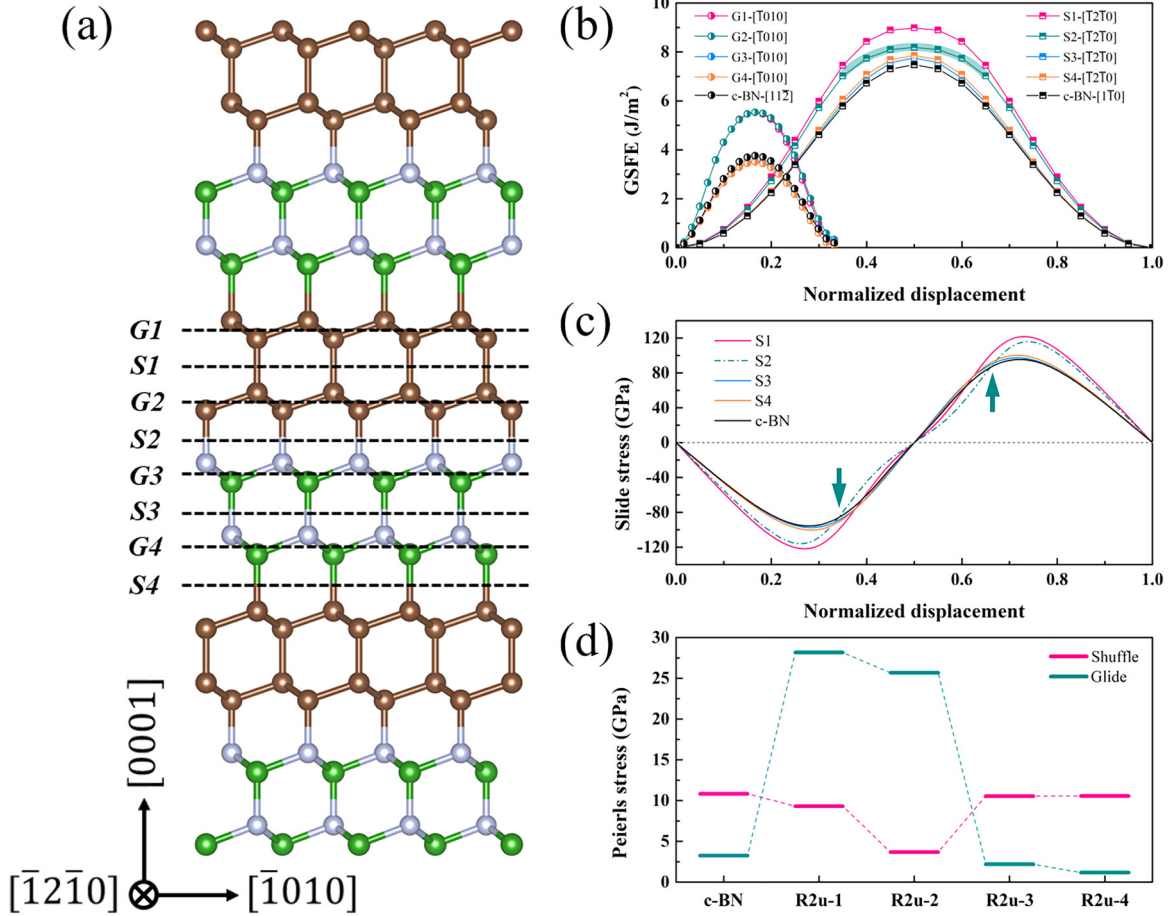
FIG. 3. (a) Topological structure of R2u−BC$_2$N with the possible weakest cleavage/slip planes marked as dotted lines. (b) GSFEs of different slip planes, (c) derived slide stress of shuffle-set planes, and (d) Peierls stress of different slip planes in R2u−BC$_2$N, together with those in c-BN shown for comparison. R2u−n (n = 1–4) in (d) represents the corresponding Peierls stress of S/G1-4.

when the stress drops, and the initial lattice configuration is transformed into a new one that exhibits mirrorlike symmetry with the original B-N layer [highlighted areas in Figs. 2(i) and 2(j)]. This unexpected inferior shear strength relative to c-BN casts a doubt on the previous conclusion of the intrinsic superhardness of BC$_2$N.

The weakest links of the R2u−BC$_2$N crystal were determined through comparing anisotropic ideal strengths along different crystallographic directions or slip systems to correlate the cleavage fracture or slip dislocation mobility, respectively [14,42,66]. As shown in Fig. 3(a), there are eight nonequivalent (001) cleavage/slip planes including four shuffle-set ("S1" to "S4") and four glide-set ("G1" to "G4") planes. The cleavage energies of shuffle-set planes are much lower than that of the glide-set planes (Fig. S3) because the vertical bonds within the shuffle-set plane are much weaker than the connected triple-bonds related to the glide-set planes when the alias tensile deformation is applied. The shuffle-set planes were further examined and a minimum ideal cleavage stress of 96.47 GPa for R2u−BC$_2$N is observed along the normal direction of "S4", which is lower than that of c-BN (99.2 GPa), suggesting its inferior decohesion resistance to c-BN.

The key descriptor representing the threshold stress that makes the dislocation move irreversibly, i.e., Peierls stress, which is ultimately linked to the hardness of a real material

[14], was analyzed thoroughly to determine the plasticity resistance. As seen in Fig. 3(b), the profiles of the generalized stacking fault energy (GSFE) of R2u−BC$_2$N agree with those of c-BN. Therefore, similar to c-BN, the unstable stacking fault energies (SFEs) of shuffle-set planes along the [$\bar{1}2\bar{1}0$] direction with the associated Peierls stress, and those of the glide-set ones along the [$\bar{1}010$] direction with the associated Peierls stress of a partial dislocation are crucial for comprehending the hardness of R2u−BC$_2$N [40]. As shown in Fig. 3(d), the lowest Peierls stress (1.17 GPa) of glide-set plane in R2u−BC$_2$N is observed in "G4" and lower than that of c-BN (3.28 GPa) because of its lower SFE compared to c-BN [Fig. 3(b)]. Surprisingly, the lowest Peierls stress of shuffle-set plane observed in "S2" is much lower than c-BN (10.13 GPa), at 3.87 GPa, which is highly unusual because the R2u−BC$_2$N has much higher SFE and slide stress in "S2" than c-BN [Figs. 3(b) and 3(c)]. By comparing the shape of their GSFE curves, a "flat peak" can be observed for R2u−BC$_2$N [green area in Fig. 3(b)], that corresponds to a "smooth turn" in its slide stress curve starting from u = 0.35 [green arrows in Fig. 3(c)]. This behavior suggests the appearance of bond softening, which may be responsible for its anomalously ultralow Peierls stress.

To gain in-depth insight into the unprecedented bond softening in R2u−BC$_2$N, we traced the bond length variations of
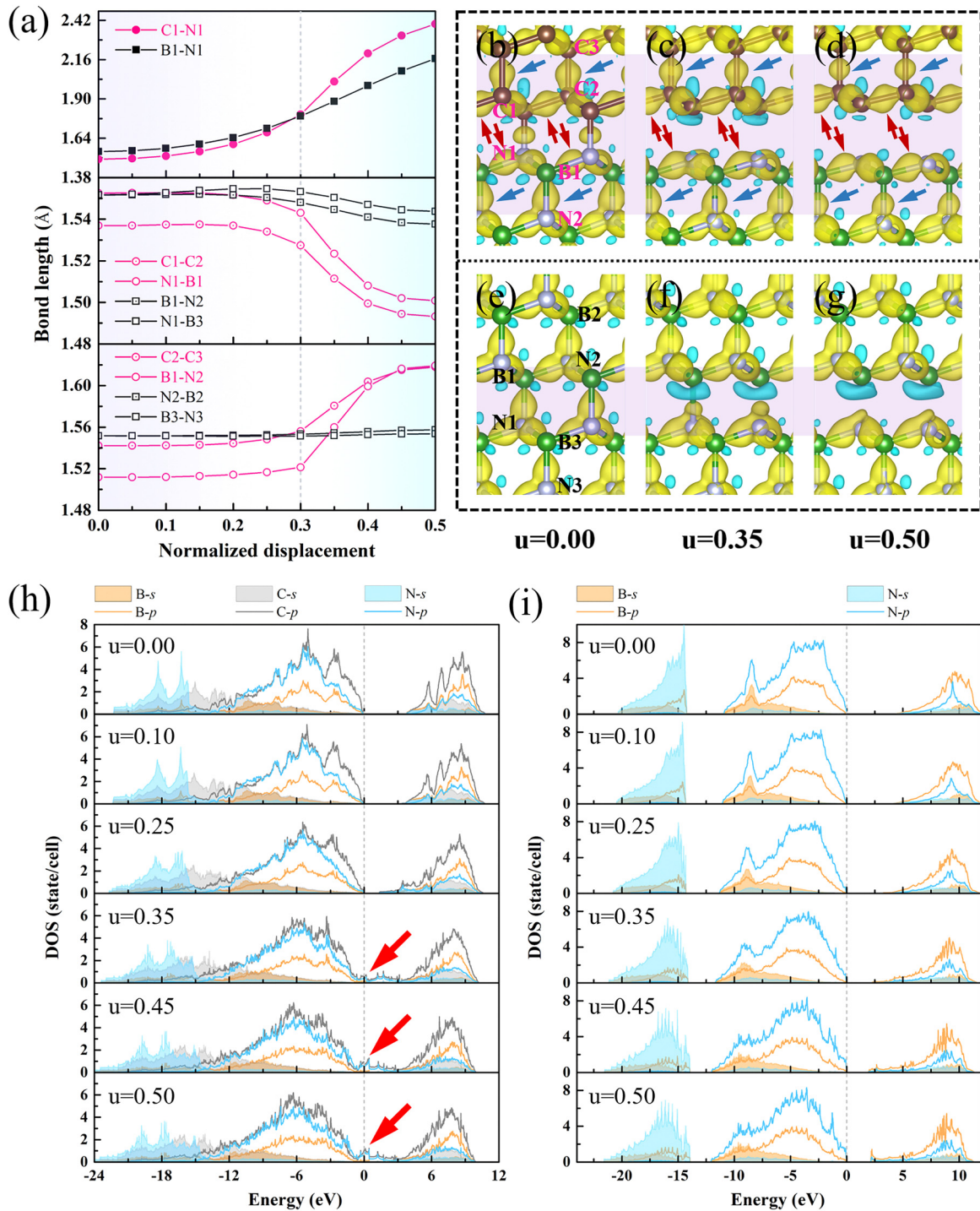
FIG. 4. (a) Bond length variations in several layers around slip plane "S2" as a function of the displacement u in R2u−BC$_2$N, compared with those in c-BN. VCDD of (b)–(d) R2u−BC$_2$N and (e)–(g) c-BN. DOS curves of (h) R2u−BC$_2$N and (i) c-BN under various displacements u. The same isosurface level of ± 0.017 electrons/Bohr^3 is used. Yellow and blue regions signify the states of charge accumulation (position) and depletion (negative), respectively. The Fermi level is set to zero. The electronic perturbations are highlighted as light purple areas in VCDDs.

several layers around the slip plane "S2" with the associated valence charge density difference (VCDD) evolutions, and compared these with those of c-BN. As shown in Fig. 4(a), when the strain increases from 0.00 to 0.30, the C1-N1 bond within "S2" in R2u−BC$_2$N remain shorter than the B1-N1 bond in c-BN, indicating the stronger bonding character of

C1-N1 bond than B1-N1 bond. After the strain of 0.30, unexpectedly, the C1-N1 bond length increases steeply to 2.40 Å at the strain of 0.50, being much longer, i.e., weaker than the B1-N1 bond (2.16 Å) in c-BN. This suggests that significant bond softening occurred in C1-N1 bond because of the large shear strain, explaining the appearance of the "flat peak" in its
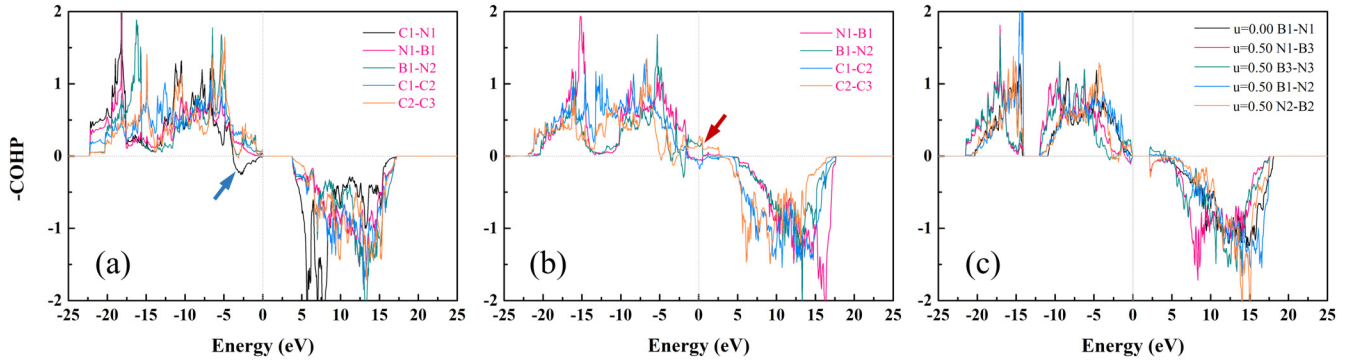
FIG. 5. COHP curves of several bonds around slip plane "S2" in $R2u-BC_2N$ under different slip displacements u: (a) $u = 0.00$, and (b) $u = 0.50$. The corresponding results for (c) c-BN are shown for comparison. The Fermi level is set to zero.

GSFE curve. Even more strikingly, similar behavior can also be found in the first and second adjacent layers to "S2", in which the surges in the bond length variations appear when the strain surpasses 0.30, whereas these bond length changes are negligible in c-BN. The notable difference in the bond length variations between $R2u-BC_2N$ and c-BN is attributed to their distinct localized charge transfer process during slipping where a wide electronic perturbation perpendicular to the "S2" is observed in $R2u-BC_2N$, involving the sequential strengthening/weakening of the bonds adjacent to C1-N1 bond [red and blue arrows in [Figs. 4(b)–4(d)]. These oscillations of bond lengths and strength represent the Friedel-like oscillations of valence charge density, shown in Figs. S4(a) and S4(b), analogous to the phenomenon found adjacent to the surfaces and interfaces of electronically perturbed solids [22,67]. As a consequence, the bond strength of C1-N1 decreases drastically, leading to its ultralow Peierls stress. While in c-BN, the charge perturbations occur predominantly within the slip plane, and rarely affect the near-neighboring atoms [Figs. 4(e)–4(g) and Figs. S4(c) and S4(d)]. Density of state (DOS) analysis reveals that the strain-induced Friedel-like oscillations accompanied by the metallization of $R2u-BC_2N$, which corresponds to the emergence of electronic states at the Fermi level after the critical shear displacement [red arrows in Fig. 4(h)]. In contrast, the band gap of c-BN decreases with increasing strain and no metallization is observed [Fig. 4(i)].

By further analyzing the crystal orbital Hamilton population (COHP) of the bonds around the slip plane in $R2u-BC_2N$, and compared with that of c-BN, a deep understanding is obtained on the aforementioned metallization. Under equilibrium condition, the C1-N1 bond of $R2u-BC_2N$ displays an antibonding fingerprint below the Fermi level [blue arrow in Fig. 5(a)], which may explain its metastable feature with respect to diamond and c-BN. After slipping along "S2", the remarkably weakened B1-N2 and C2-C3 bonds caused by the Friedel-like oscillations, exhibit large bonding states around the Fermi level [red arrow in Fig. 5(b)]. These fascinating bonding features indicate that, as the B1-N2 and C2-C3 bonds weaken, the energy of the bonding states increases and that of the antibonding ones decreases, resulting in the closure of the energy gap. This drives the localized bonding electrons around "S2" into a delocalized antibonding state, thereby eliciting the metallization. In comparison, no bonding states are found in c-BN that cross the Fermi level

[Fig. 5(c)]. It is noted that these oscillations do not occur when slipping in the weakest glide-set plane "G4" in $R2u-BC_2N$. As shown in Figs. S5(a)–S5(g), the bond length variations and charge distributions around "G4" in $R2u-BC_2N$ are essentially equivalent to those in c-BN. Therefore, no metallization is found in either $R2u-BC_2N$ or c-BN [Figs. S5(h) and S5(i)], while a lower Peierls stress than c-BN is mainly attributed to the lower intrinsic bonding strength of N1-B1 bond within "G4" than that of the N1-B1 bond in c-BN, because as the strain increases, the latter becomes more shorter and stronger than the former. Besides, different from the Friedel oscillations observed to occur in Ti-Si-N nanocomposites systems [68,69] at equilibrium and leads to poor strength under uniform strain, the metallization in $R2u-BC_2N$ does not occur under these conditions (Fig. S6), which explains its ideal shear strength is only slightly lower than that of c-BN.

Based on the aforementioned investigations on the intrinsic mechanical properties of $R2u-BC_2N$, it can be concluded that $R2u-BC_2N$ cannot be ranked as the intrinsic super-hard material superior to c-BN, due to its lower ideal shear strength, weaker interplanar cleavage, and dislocation slip resistance. This conclusion strongly challenges the previous conclusion on the superhardness of BC_2N based on the intrinsic mechanical strength [11,12,20]. The microscopic origin of nanostructured BC_2N materials was further investigated using large-scale molecular dynamics simulations. According to experimental information, the BC_2N materials with a nanocrystalline structure adhered together by carbon amorphous interfacial layer (AIL) with varying thicknesses (illustrated in Fig. S7) were constructed and then loaded by uniaxial stress. Compared with the BC_2N nanostructure without AIL, the dislocation nucleation and penetration at grain boundaries reduced considerably in the BC_2N nanostructure containing a 1-nm-thick AIL [Figs. S7(b) and S7(c)]. As the thickness of AIL increases to 2 nm [Fig. S7(d)], such as that in the experimentally synthesized sample [8], almost no lattice dislocations are observed, indicating that the deformation mechanism switched from lattice dislocation to interface sliding. This phenomenon is consistent with that observed in the nanostructured diamond and metallic materials [15,70,71]. Hence, the amorphous boundary is verified as being primarily responsible for the experimentally observed extreme hardness of BC_2N.

In summary, through evaluating the XRD patterns, and pressure-dependent thermodynamic, mechanical, and phonon stabilities, we identified the experimentally synthesized BC_2N phase as $R2u-BC_2N$. We further uncovered a nontraditional bond deformation mechanism mediated by a peculiar strain-driven electronic behavior. After the critical shear strain, owing to the appearance of metallization, Friedel-like oscillations of valence charge density intensely weaken the heterogenous bonds across the slip plane, thus remarkably limiting the dislocation slip resistance of $R2u-BC_2N$. The interfacial amorphous carbon, rather than the crystal's inside, predominantly contributes to its measured extreme hardness. Our ongoing work suggest that such oscillations are likely to be a ubiquitous phenomenon that occurs also in other (111) superlattice boron carbon nitrides, e.g., BC_4N [72,73] and $BC_{10}N$ [74], which remind us that avoiding these oscillations through combining nanostructure engineering and grain boundary engineering is necessary to achieve superior hardness of B-C-N materials.

[1] S. Nakano, M. Akaishi, T. Sasaki, and S. Yamaoka, Chem. Mater. **6**, 2246 (1994).

[2] E. Knittle, R. B. Kaner, R. Jeanloz, and M. L. Cohen, Phys. Rev. B **51**, 12149 (1995).

[3] T. Komatsu, M. Nomura, Y. Kakudate, and S. Fujiwara, J. Mater. Chem. **6**, 1799 (1996).

[4] R. B. Kaner, J. J. Gilman, and S. H. Tolbert, Science **308**, 1268 (2005).

[5] Z. S. Zhao, B. Xu, and Y. J. Tian, Annu. Rev. Mater. Res. **46**, 383 (2016).

[6] X. T. Ren, X. Z. Yan, L. P. Wang, Y. S. Zhao, and S. M. Wang, J. Superhard Mater. **43**, 307 (2021).

[7] V. L. Solozhenko, D. Andrault, G. Fiquet, M. Mezouar, and D. C. Rubie, Appl. Phys. Lett. **78**, 1385 (2001).

[8] Y. Zhao, D. W. He, L. L. Daemen, T. D. Shen, R. B. Schwarz, Y. Zhu, D. L. Bish, J. Huang, J. Zhang, G. Shen *et al.*, J. Mater. Res. **17**, 3139 (2002).

[9] C. Chen and H. Sun, Phys. Rev. Lett. **99**, 159601 (2007).

[10] S. Chen, X. G. Gong, and S. H. Wei, Phys. Rev. Lett. **99**, 159602 (2007).

[11] Z. Pan, H. Sun, and C. Chen, Phys. Rev. Lett. **98**, 135505 (2007).

[12] S. Chen, X. G. Gong, and S. H. Wei, Phys. Rev. Lett. **98**, 015502 (2007).

[13] Y. Zhang, H. Sun, and C. Chen, Phys. Rev. Lett. **93**, 195504 (2004).

[14] R. F. Zhang, S. H. Zhang, Y. Q. Guo, Z. H. Fu, D. Legut, T. C. Germann, and S. Veprek, Phys. Rep. **826**, 1 (2019).

[15] Q. Zhang, C. Wang, H. Zhang, S. Zhang, Z. Liu, D. Legut, S. Veprek, and R. Zhang, Carbon **170**, 394 (2020).

[16] H. Sun, S. H. Jhi, D. Roundy, M. L. Cohen, and S. G. Louie, Phys. Rev. B **64**, 094108 (2001).

[17] X. F. Zhou, J. Sun, Y. X. Fan, J. Chen, H. T. Wang, X. Guo, J. He, and Y. Tian, Phys. Rev. B **76**, 100101(R) (2007).

[18] X. F. Zhou, J. Sun, Q. R. Qian, X. Guo, Z. Liu, Y. Tian, and H. T. Wang, J. Appl. Phys. **105**, 093521 (2009).

[19] Q. Li, M. Wang, A. R. Oganov, T. Cui, Y. Ma, and G. Zou, J. Appl. Phys. **105**, 053514 (2009).

[20] L. Liu, Z. Zhao, T. Yu, S. Zhang, J. Lin, and G. Yang, J. Phys. Chem. C **122**, 6801 (2018).

[21] S. Zheng, R. Zhang, R. Huang, T. Taniguchi, X. Ma, Y. Ikuhara, and I. J. Beyerlein, Appl. Phys. Lett. **109**, 081901 (2016).

[22] R. F. Zhang, A. S. Argon, and S. Veprek, Phys. Rev. Lett. **102**, 015503 (2009).

[23] D. Roundy and M. L. Cohen, Phys. Rev. B **64**, 212103 (2001).

[24] S. H. Zhang, Z. H. Fu, and R. F. Zhang, Comput. Phys. Commun. **238**, 244 (2019).

[25] B. Joos, Q. Ren, and M. S. Duesbery, Phys. Rev. B **50**, 5890 (1994).

[26] Y. Q. Guo, S. H. Zhang, I. J. Beyerlein, D. Legut, S. L. Shang, Z. K. Liu, and R. F. Zhang, Acta Mater. **181**, 423 (2019).

[27] M. Mattesini and S. F. Matar, Intl. J. Inorgan. Mater. **3**, 943 (2001).

[28] X. Luo, X. Guo, B. Xu, Q. Wu, Q. Hu, Z. Liu, J. He, D. Yu, Y. Tian, and H. T. Wang, Phys. Rev. B **76**, 094103 (2007).

[29] X. G. Luo, X. J. Guo, Z. Y. Liu, J. L. He, D. L. Yu, B. Xu, Y. J. Tian, and H. T. Wang, Phys. Rev. B **76**, 092107 (2007).

[30] Z. J. Wu, E. J. Zhao, H. P. Xiang, X. F. Hao, X. J. Liu, and J. Meng, Phys. Rev. B **76**, 054115 (2007).

[31] S. H. Zhang and R. F. Zhang, Comput. Phys. Commun. **220**, 403 (2017).

[32] See Supplemental Material at http://link.aps.org/supplemental/10.1103/PhysRevB.106.L060101 for further details on the methods used in this study, additional figures and table. the Supplemental Material also includes Refs. [14,24,25,31,33–63].

[33] G. Kresse and J. Furthmüller, Phys. Rev. B **54**, 11169 (1996).

[34] G. Kresse and D. Joubert, Phys. Rev. B **59**, 1758 (1999).

[35] D. M. Ceperley and B. J. Alder, Phys. Rev. Lett. **45**, 566 (1980).

[36] J. P. Perdew and A. Zunger, Phys. Rev. B **23**, 5048 (1981).

[37] M. P. A. T. Methfessel and A. T. Paxton, Phys. Rev. B **40**, 3616 (1989).

[38] H. J. Monkhorst and J. D. Pack, Phys. Rev. B **13**, 5188 (1976).

[39] A. Togo and I. Tanaka, Scr. Mater. **108**, 1 (2015).

[40] S. H. Zhang, D. Legut, T. C. Germann, S. Veprek, H. J. Zhang, and R. F. Zhang, Phys. Rev. B **101**, 014104 (2020).

[41] S. H. Zhang, I. J. Beyerlein, D. Legut, Z. H. Fu, Z. Zhang, S. L.

Shang, Z. K. Liu, T. C. Germann, and R. F. Zhang, Phys. Rev. B **95**, 224106 (2017).

[42] S. H. Zhang, X. Zheng, Q. Q. Jin, S. J. Zheng, D. Legut, X. H. Yu, H. Y. Gou, Z. H. Fu, Y. Q. Guo, B. M. Yan *et al.*, Phys. Rev. Mater. **2**, 123602 (2018).

[43] S. H. Zhang, D. Legut, and R. F. Zhang, Comput. Phys. Commun. **240**, 60 (2019).

[44] A. T. Blumenau, R. Jones, T. Frauenheim, B. Willems, O. I. Lebedev, G. Van Tendeloo, D. Fisher, and P. M. Martineau, Phys. Rev. B **68**, 014115 (2003).

[45] Y. Kamimura, K. Edagawa, A. M. Iskandarov, M. Osawa, Y. Umeno, and S. Takeuchi, Acta Mater. **148**, 355 (2018).

[46] Z. R. Liu, B. N. Yao, and R. F. Zhang, Comput. Mater. Sci. **210**, 111027 (2022).

[47] G. Voronoi, J. Reine Angew. Math. **134**, 198 (1908).

[48] C. de Tomas, I. Suarez. Martinez, and N. A. Marks, Carbon **109**, 681 (2016).

[49] J. Tersoff, Phys. Rev. B **49**, 16349 (1994).

[50] C. Huang, X. Peng, B. Yang, H. Xiang, S. Sun, X. Chen, Q. Li, D. Yin, and T. Fu, Carbon **132**, 606 (2018).

[51] C. Huang, X. Peng, and B. Yang, Ceram. Int. **47**, 28659 (2021).

[52] C. Huang, X. Peng, B. Yang, S. Weng, Y. Zhao, and T. Fu, Comput. Mater. Sci. **157**, 67 (2019).

[53] Y. Liu, B. Li, and L. Kong, Comput. Mater. Sci. **148**, 76 (2018).

[54] S. Plimpton, J. Comput. Phys. **117**, 1 (1995).

[55] W. G. Hoover, Phys. Rev. A **31**, 1695 (1985).

[56] W. G. Hoover, Phys. Rev. A **34**, 2499 (1986).

[57] A. Stukowski, Model. Simul. Mater. Sci. Eng. **18**, 015012 (2010).

[58] B. N. Yao and R. F. Zhang, Comput. Phys. Commun. **247**, 106857 (2020).

[59] S. Maintz, V. L. Deringer, A. L. Tchougréeff, and R. Dronskowski, J. Comput. Chem. **37**, 1030 (2016).

[60] R. Nelson, C. Ertural, J. George, V. L. Deringer, G. Hautier, and R. Dronskowski, J. Comput. Chem. **41**, 1931 (2020).

[61] R. Dronskowski and P. E. Blöchl, J. Phys. Chem. C **97**, 8617 (1993).

[62] V. L. Deringer, A. L. Tchougréeff, and R. Dronskowski, J. Phys. Chem. A **115**, 5461 (2011).

[63] J. A. Zimmerman, C. L. Kelchner, P. A. Klein, J. C. Hamilton, and S. M. Foiles, Phys. Rev. Lett. **87**, 165507 (2001).

[64] Y. Zhang, H. Sun, and C. Chen, Phys. Rev. B **73**, 144115 (2006).

[65] S. Zhang, D. Legut, Z. Fu, T. C. Germann, and R. Zhang, Carbon **137**, 156 (2018).

[66] C. Lu, Q. Li, Y. Ma, and C. Chen, Phys. Rev. Lett. **119**, 115503 (2017).

[67] J. Friedel, Philos. Mag. **43**, 153 (1952).

[68] S. Hao, B. Delley, and C. Stampfl, Phys. Rev. B **74**, 035424 (2006).

[69] R. F. Zhang, A. S. Argon, and S. Veprek, Phys. Rev. B **79**, 245426 (2009).

[70] V. Turlo and T. J. Rupert, Acta Mater. **151**, 100 (2018).

[71] G. Wu, K. Chan, L. Zhu, L. Sun, and J. Lu, Nature (London) **545**, 80 (2017).

[72] S. Y. Chen, X. G. Gong, and S. H. Wei, Phys. Rev. B **77**, 014113 (2008).

[73] X. G. Luo, X. F. Zhou, Z. Y. Liu, J. L. He, B. Xu, D. L. Yu, H. T. Wang, and Y. J. Tian, J. Phys. Chem. C **112**, 9516 (2008).

[74] W. C. Chen, J. N. Schmidt, D. Yan, Y. K. Vohra, and C. C. Chen, npj Comput. Mater. **7**, 114 (2021).